JOURNAL OF THERMOPHYSICS AND HEAT TRANSFER
Vol. 20, No. 2, April–June 2006

Modeling and Experimental Assessment of CN Radiation Behind a Strong Shock Wave

Deepak Bose,* Michael J. Wright,† David W. Bogdanoff,‡ George A. Raiche,§ and Gary A. Allen Jr.¶
NASA Ames Research Center, Moffett Field, California 94035

Assessment of nonequilibrium thermochemical models for shock-layer radiation in N_2/CH_4 mixtures is presented via comparisons with spectrally and temporally resolved intensity measurements from a set of shock tube experiments. The experiments were carried out at the Electric Arc Shock Tube facility at NASA Ames Research Center in a rarified environment [13.3–133.3 Pa (0.1 and 1 torr)] representative of the peak heating conditions of a Titan aerocapture trajectory (5–9 km/s). The baseline model that assumes a Boltzmann population of the CN excited states consistently overpredicts the shock-layer radiation intensity at lower pressure [13.3 Pa (0.1 torr)]. A nonlocal collisional radiative model that solves a simplified master equation and includes radiative transport and nonlocal absorption in the shock tube is presented. The proposed model improves the prediction of the nonequilibrium radiation overshoot peak, but still underpredicts the intensity decay rate in the low-pressure case. Further analysis suggests possible reasons for the remaining disagreement, the most likely being a slow CN consumption in the current chemical kinetics model in the intensity fall-off region.

I. Introduction

NASA'S In-Space Propulsion (ISP) program is currently considering the viability of an aerocapture mission to Saturn's largest moon, Titan.[1] Titan has an atmosphere that is unique in the solar system in that it consists primarily of nitrogen, with small amounts of methane (2–5% by mole) and argon (0–8% by mole) (Ref. 2). However, the recent Cassini flybys have indicated an atmosphere consisting of about $1.8 \pm 0.5\%$ CH_4 by volume at entry altitudes. Prior studies[3–6] of Titan aerocapture aeroheating, assuming a blunt 70-deg sphere–cone geometry flying at angle of attack and a set of bounding entry trajectories with entry speeds between 6–10 km/s, have shown that the heating of the vehicle will be dominated by radiation produced in the hot shock layer and transmitted to the surface. Furthermore, it has been predicted that, below an entry speed of about 7 km/s, nearly all of the radiative heating is due to spontaneous de-excitation of CN molecules from excited electronic states, chief among them the violet ($B^2\Sigma^+ \rightarrow X^2\Sigma^+$) and the red ($A^2\Pi \rightarrow X^2\Sigma^+$) bands. The CN radical is a strong radiator and also contributes significantly to radiative heating rates during entries to both Mars and Venus, which have CO_2/N_2 atmospheres. However, CN radiation is of particular concern for Titan entries because significant amounts of CN form when the methane in the atmosphere is dissociated by the shock wave and the freed carbon atoms react with the abundant atmospheric nitrogen. The amount of radiation produced is significantly enhanced in the nonequilibrium portion of the shock wave, a well-known phenomena discussed extensively in the literature.[7,8]

Figure 1a shows freestream velocity and pressure vs time for one of the design trajectories used in the Titan aerocapture analysis of Ref. 6. For this case, the peak freestream pressure is only about 15 Pa (0.113 torr) for an entry velocity of 6.5 km/s. Figure 1b shows the computed stagnation point convective and radiative heat transfer rate for this case.[6] The predicted peak radiative heat flux is about four times the peak convective heat flux and occurs at about $t = 270$ s, at a velocity of 5.4 km/s, and a freestream pressure of 11 Pa (0.083 torr). Clearly, if these predictions are accurate, the thermal protection system (TPS) for this mission would be selected and sized based primarily on the radiative heating environment.[9]

The radiation from the excited states of CN is dependent on the rate at which these states are populated and depopulated via collisions and radiative transitions. A model for the collisional excitation of CN is, therefore, required to predict the emission from the shock layer and the resulting radiative heat flux. Unfortunately, no experimentally validated model for radiative emission power from a N_2/CH_4 shock layer currently exists. Therefore, the prior analyses for Titan aerocapture assumed a Boltzmann distribution, governed by the mixture vibrational temperature, to describe the populations of CN electronic states. The details and limitations of this assumption will be discussed in a later section. A Boltzmann assumption was used because it was deemed likely to provide a conservative upper limit on the amount of radiation generated by CN. However, the accuracy of this assumption is not known, primarily due to a lack of experimental data in the open literature to validate the physical models employed in the simulations. This lack of validation data results in large uncertainties in the predicted heat fluxes and loads on the entry vehicle, which equates to increased risk and/or TPS system mass for any such mission.

Radiative heating from the CN molecule was also of concern during the design of the ESA's Huygens probe,[10–12] which successfully entered the atmosphere of Titan on 14 January 2005. Peak radiative heat fluxes for the Huygens probe were predicted to exceed 90 W/cm^2 on the worst-case design trajectories, more than twice the convective heat flux.[11] The maximum radiative heating was predicted to occur at approximately $V_\infty \sim 5.1$ km/s and $p_\infty \sim 15$ Pa (0.113 torr) (Ref. 11), conditions that are very similar to those of the peak heating point of the Titan aerocapture vehicle.

Several experimental and computational studies were performed during the design of the Huygens probe in an attempt to better characterize the dynamics of CN emission. Park[13] and Park and Bershader[14] conducted a series of shock tube tests in a $N_2/CH_4/Ar$ mixture at Stanford University. These tests were all conducted at a nominal shock velocity of 5.75 km/s and an ambient pressure of 266 Pa (2 torr). Calibrated intensities were measured as a function of time at specific wavelengths using photomultiplier tubes. Park used a master equation for CN excited states to analyze the data. However,

Presented as Paper 2005-768 at the AIAA 43rd Aerospace Sciences Meeting and Exhibit, Reno, NV, 10–13 January 2005; received 28 March 2005; revision received 21 June 2005; accepted for publication 22 June 2005.

*Senior Research Scientist, Ion American Corporation; bosedeepak@hotmail.com. Member AIAA.
†Senior Research Scientist. Senior Member AIAA.
‡Senior Research Scientist, ELORET Corporation. Associate Fellow AIAA.
§Senior Research Scientist, Reacting Flow Environments Branch. Member AIAA.
¶Senior Research Scientist, ELORET Corporation. Member AIAA.

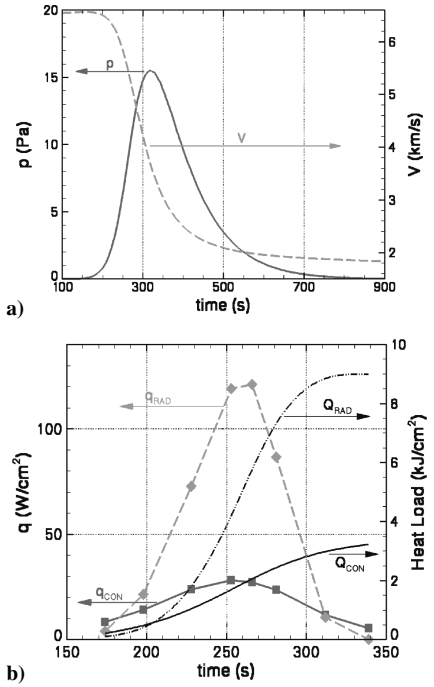

Fig. 1 Trajectory profiles: a) Freestream pressure and velocity as function of time for representative trajectory used for design of Titan aerocapture vehicle and b) computed stagnation point convective q^C and radiative q^R heat flux and heat load on Titan aerocapture vehicle along trajectory (results from Ref. 6).

because they did not compare the absolute intensities, the validity of their master equation formulation remains unknown. Also, the test data and comparisons were made at a higher pressure than what is of interest at the peak heating conditions where the nonequilibrium effects were smaller. Labracherie et al.[15] and Kpante et al.[16] studied the radiative emission of CN in a series of shock tube tests at the TCM2 free piston facility in Marseille, France. These tests were conducted at a range of velocities and gas compositions appropriate for Huygens, but the ambient pressure was on the order of 200 Pa (1.5 torr). Photomultiplier tubes were again the primary instrumentation and provided uncalibrated intensities as a function of time at specific wavelengths. An optical multichannel analyzer was also employed to provide a spectrally resolved intensity distribution at a single time point. Kpante et al.[16] analyzed these data and showed reasonable agreement between the experimentally observed overshoot and fall-off timescales using computations assuming a Boltzmann distribution of CN excited states at the vibrational temperature. However, absolute intensities could not be compared because the experimental data for this test series were not calibrated. Later, Ramjaun et al.[17] performed additional shock tube tests at the Marseille facility and compared their uncalibrated data with simulations on a relative scale. More recently Zalogin et al.[18] conducted a series of shock tube tests in $CO_2/N_2/Ar$ gas mixtures at velocities between 3 and 4 km/s and pressures from 66 to 660 Pa (from 0.5 to 5 torr). This experiment, although for a different mixture, was used to estimate the collisional excitation and deexcitation rates of CN based on a simplified master equation for CN excited states. Unfortunately, all of these shock tube test series were conducted at pressures that were about an order of magnitude higher than the peak heating point on both the Huygens probe and the proposed Titan aerocapture vehicle. At these higher pressures, nonequilibrium effects would be much smaller, making validation of a nonequilibrium radiation model appropriate for flight predictions based on these data very difficult. Also, the majority of the data from these tests measured the emission at a single wavelength as a function of time, instead of the total integrated radiative power over a large wavelength range needed to validate and calibrate computational models.

Because these shock tube experiments were insufficient to build and validate a complete model of CN emission in a nonequilibrium environment, recently a new series of shock tube tests were performed at the Electric Arc Shock Tube (EAST) facility at the NASA Ames Research Center. The tests were performed at velocities, pressures, and gas compositions representative of the entry conditions of the Titan aerocapture vehicle. Spectrally and spatially resolved intensities from these shots were recorded over a wide wavelength range by imaging two separate spectrographs, and the resulting data were calibrated to provide absolute intensity measurements. Further details of the experimental setup, instrumentation, and intensity calibration procedure are discussed in the next section. The resulting intensities are compared to simulations of the shock tube experiments using the same codes and physical models employed in previous simulations of the Titan aerocapture flight environment. A new collisional radiative model is proposed based on the collisional excitation rates estimated by Zalogin et al.[18] for the CN violet system. However, significant discrepancies between simulation and test data remain, especially at lower pressure (0.1 torr) when the nonequilibrium effects are large. Although the peak intensity in the nonequilibrium region can be predicted within a factor of two, the observed radiation intensity fall off is much faster than what the models predict. We suggest possible missing mechanisms that would likely explain the discrepancy. Further investigations, a reassessment of the gas-phase chemistry, excited state chemistry, and uncertainty analysis are needed to build a CN radiation model suitable for flight radiative heating predictions with reasonable uncertainty bounds. Investigation should also be directed to ensure adequate ground to flight traceability, which requires physical models with sufficient maturity to distinguish and identify phenomena that might make ground-based estimates less conservative.

II. EAST Measurements

A. Facility and Test Conditions

The experiments were carried out in the EAST at NASA Ames Research Center. This facility is a 10.16-cm-diam shock tube with an electric arc-heated driver. Figure 2 shows the facility. The arc in the driver is supported by a capacitor bank, which can store up to 1.24 MJ of energy at 40 kV. The driver gas is usually hydrogen, helium, or helium/argon mixtures. Reflected shock pressures up to 50 MPa (375 torr) can be obtained. Shock velocities ranging from 1.5 to 46 km/s have been obtained. Further description of the facility is given in Refs. 19 and 20.

For the present experiments, the facility was configured as follows. A conical driver with a volume of 1292 cm^3 was used. The driver gas was either a 93.2%He/6.8%Ar mixture or pure He. The driver gas fill pressure was 6.8 atm, and a 0.305-mm-thick aluminum main diaphragm was used. The driver capacitor bank was set up with a capacitance of 1530 μF and bank voltages of 8–25 kV were used, depending on the test conditions desired. For some tests, a 7.62-cm-long buffer gas region was used between the driver and the driven tube to increase the test time. The buffer was filled with Ar at pressures of 1.1 or 2.2 atm, and an aluminum diaphragm 0.10–0.18 mm thick was used between the buffer and the driven tube. The center of the spectrograph windows of the test section was 7.57 m from the main diaphragm.

Five different premixed $N_2/CH_4/Ar$ gas mixtures were used to simulate the Titan atmosphere. The driven tube fill pressures were 13.3 and 133.3 Pa (0.1 and 1.0 torr) at room temperature. Shock velocities ranged from 5 to 9 km/s. A few tests at higher pressure (133.3 Pa) and higher speeds (7–9 km/s) than what is expected

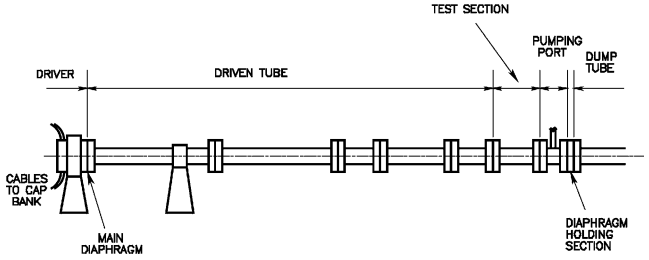

Fig. 2 NASA Ames Research Center EAST configured for Titan atmosphere radiation tests.

at the peak heating conditions were done to build thermochemical models with wider range of applicability. Tests with air and nitrogen-driven tube gases were also made to compare the data with an earlier series of tests done in the same facility.[21,22] These tests were made with 133.3 Pa (1.0 torr) nitrogen at shock velocity of ~6 km/s and with 13.3 Pa (0.1 torr) air at a shock velocity of ~10 km/s. Test times (before arrival of driver gas contamination) were >16 μs for tests at a driven gas fill pressure of 133.3 Pa (1 torr). For a driven gas fill pressure of 13.3 Pa (0.1 torr), test times were 8–12, 2–6, and 0–4 μs for shock velocities of ~6, 8–9, and ~10 km/s, respectively. The arrival of driver gas was determined mainly by the time of the appearance, in the spectrographs, of tungsten lines from the driver arc trigger wire. The arrival of the driver gas was also evident by a sudden change in the slopes of the intensities in two spectrograph images that were taken for each test. Also, these slope changes in two images occur at nearly the same physical location, as will be evident from the profiles presented at a later section, indicating the arrival of the contact surface.

There were 40 test runs made in the Titan entry radiation test entry; 33 of these runs provided useful spectral data.

B. Instrumentation

Six PCB Model 113A21 quartz crystal pressure tranducers are located in ports along the driven tube. These transducers provide the primary measurement of shock velocity. The shock velocity is found to decrease slightly as it moved along the tube. The test velocity is determined from the two transducers on either side of the test section. Four broadband photomultiplier tubes (1P21, 1P28, or Hamamatsu R456 tubes) were located just outside of ports along the driven tube. Three monochromators were located facing windows in ports in the test section near the spectrographs. Two of these monochromators were Bausch and Lomb 0.25-m instruments with 600 grooves/mm gratings. These were operated at various wavelengths from 315 to 777 nm. The third was a McPherson Model 218 0.3-m instrument with a 1200 grooves/mm grating. This latter instrument was operated in the UV and vacuum UV at wavelengths from 165 to 247 nm. None of the optical instruments just discussed were calibrated.

The two spectrographs were McPherson model 218 0.3-m scanning monochromators operated as spectrographs by removing the exit slits and mounting intensified charge-coupled device (ICCD) cameras at the exit slit location. Inlet slit widths of 30 and 60 μm were used. A number of gratings from 150 to 2400 grooves/mm were used. Filters were used at the inlet slits of the spectrographs to eliminate second-order spectral lines. One spectrograph (the blue or short-wavelength spectrograph) was operated with center wavelengths from 269 to 521 nm with wavelength spans of ~180, 33, and 14 nm for low, medium, and high-resolution gratings. The second spectrograph (the red or long-wavelength spectrograph) was operated with center wavelengths of from 590 to 772 nm with wavelength spans of 226 and 22 nm for low- and high-resolution gratings. The experimental setup of one spectrograph is shown in Fig. 3. The second spectrograph was placed on the opposite side of the test section from the spectrograph shown in Fig. 3. The windows in the test section facing the spectrographs were 11.4 cm long and 0.89 cm wide.

Roper Scientific PI.MAX ICCD cameras were used to record the spectral images. For the blue spectrograph, a model PI.MAX: 1024UV camera was used, with 1024 × 256 pixels and sensitivity from 115 to 870 nm. For the red spectrograph, a model PI.MAX: 512HQ camera was used, with 512 × 512 pixels and sensitivity from 480 to 900 nm. The exposures for the cameras ranged from 0.25 to 1.5 μs, with most tests being made with exposures of 1.0 μs or less. The timing of the camera exposures were chosen to place the shock wave about 70–80% of the way across the test section window. The two ICCD images obtained in each test run have wavelength in one direction and distance behind (or in front of) the shock wave in the other direction. The camera for the blue spectrograph was oriented so that the 1024 pixels were in the wavelength direction.

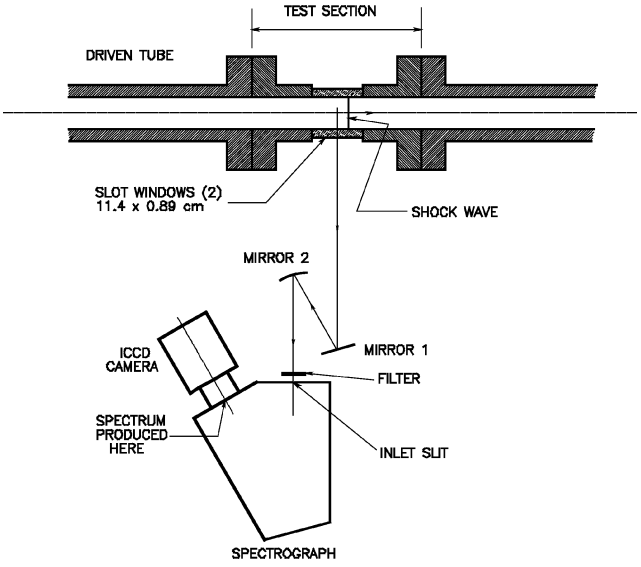

Fig. 3 Spectrograph setup.

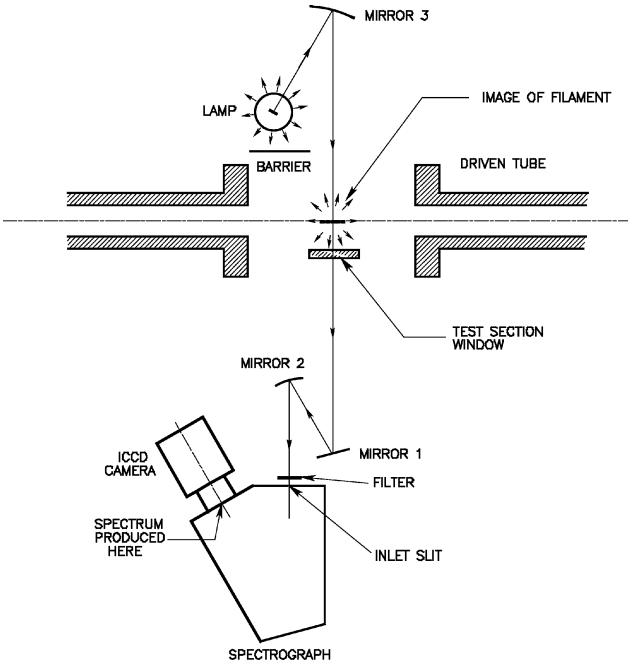

Fig. 4 Spectrograph setup for lamp calibration.

C. Data Reduction, Accuracy, Reproducibility, and Comparison with Earlier Work

The images obtained directly form the ICCD cameras are in the form of "counts" (up to a maximum of ~65,000) for each pixel. To convert the data for the Titan atmosphere tests into absolute intensities (W/cm^2-str-μ), the cameras were calibrated. Calibration was done using the setup shown in Fig. 4. The test section was removed, and a calibrated tungsten ribbon lamp was set up on the opposite side of the driven tube from the spectrograph. With the use of a concave mirror, a ~3.5× magnified image of the lamp filament was created on the centerline of the test section. When this arrangement was used, calibrations were made of all 12 spectrograph configurations. For each configuration, spectra were taken at each of seven filament positions. Partially automated computer analysis procedures were developed to allow the lamp spectra data to be used to convert the raw Titan atmosphere radiation data into absolute radiation intensity data.

The shock velocities, measured between two pressure transducers at either end of the test section, were measured with maximum

errors of ±1%. The light intensities of individual pixels of the ICCD images of the spectra have estimated errors of ±30% or less, due to the noise inherent in the necessary high-gain operating condition of the ICCD cameras. When the data from the cameras are averaged over either the wavelength or the spatial distance directions, or both, these errors will be reduced. As is typical for electric-arc driven shock tubes, the shock velocities obtained for nominally identical facility operating conditions showed a variation of ±5%. For example, of the eight tests made with 8.6% CH_4 at a driven tube fill pressure of 13.3 Pa (0.1 torr), seven of the tests had shock velocities of 5.83–6.03 km/s and one had a shock velocity of 5.47 km/s.

One test run was made with 133.3 Pa (1.0 torr) nitrogen at a shock velocity of ~6 km/s, and four test runs were made with 13.3 Pa (0.1 torr) air at a shock velocity of ~10 km/s. The purpose of these tests was to compare results from the present facility test entry with earlier entries (reported in Refs. 21 and 22) in the same facility. The differences in the measured intensities between the two tests in the equilibrium and nonequilibrium portions of the shock layer was consistently found to be within 20–30%, which can be attributed to the shock velocity differences in the tests.

D. Measured Data

Figure 5a and 5b show two sample spectrograph (blue spectrograph) images from two of the shots. Similar images were taken in the red spectrograph for larger wavelengths in all shots. Figures 5 show intensity variations at different wavelengths with distance along the shock tube axis. The shock front and the major band systems are identified. Figure 5a shows the three major vibrational manifolds of the CN (violet) system. The faint lines on either side are also CN (violet) manifolds with $|\Delta v|>1$, where v is the vibrational level. A C_2 (Swan) feature is visible at the right side of the image. CN (violet) bands dominate the postshock spectrum. Note that the color maps of these images have been adjusted by saturating the intense lines and spreading the color in the logarithmic scale to see the faint lines. A small amount of radiation is also evident ahead of the shock front. This signal is either due to precursor ionization, which is likely to emit N_2^+ (first negative) signal, or it may simply be due to the diffuse reflections of the CN (violet) signal from the shock tube walls. Figure 5b shows a high-resolution image of the $\Delta v = -1$ vibrational manifold of the CN (violet) system. Figure 5b shows the individual vibrational band heads, which can be used to estimate vibrational and rotational temperatures of the CN (B) state. The tungsten lines, indicating the arrival of driver gas contamination, are also visible.

Figures 6a–6c show the spectral scans derived at the peak intensity location from the spectrograph images. The calibrated absolute intensities are presented. CN (violet) is seen to be the dominant band followed by CN (red) and C_2 (Swan) bands. These data confirm earlier predictions[4,6] which showed CN (violet) to be the brightest system at 5–6 km/s of shock speed. The details of the experimental data will be presented in a separate publication. The uncertainty in the integrated intensities is deemed to be less than 20%, although the uncertainty in the spectrally resolved data may be larger.

III. Baseline Shock-Layer Simulations

The shock-tube simulations are performed using the computational fluid dynamics (CFD) code DPLR,[23] modified to enable one-dimensional shock tube calculations. The DPLR code has been used for many previous planetary entry simulations and was one of the primary tools used to predict the flight aeroheating environment for the ISP Titan aerocapture mission concept.[3,6] Each shock tube simulation is initialized using the perfect gas shock jump conditions based on the known driver gas T, p, chemical composition, and the measured shock velocity V_s in the test window. The gas composition and internal energy modes (other than rotation) are assumed frozen immediately behind the shock to initialize the first point in the postshock region. The downstream flowfield is then computed by a space-marching solution of the one-dimensional Euler equations,

$$\frac{\partial \boldsymbol{F}(x)}{\partial x} = \boldsymbol{W}(x), \qquad \boldsymbol{U}(x) = f[\boldsymbol{F}(x)] \tag{1}$$

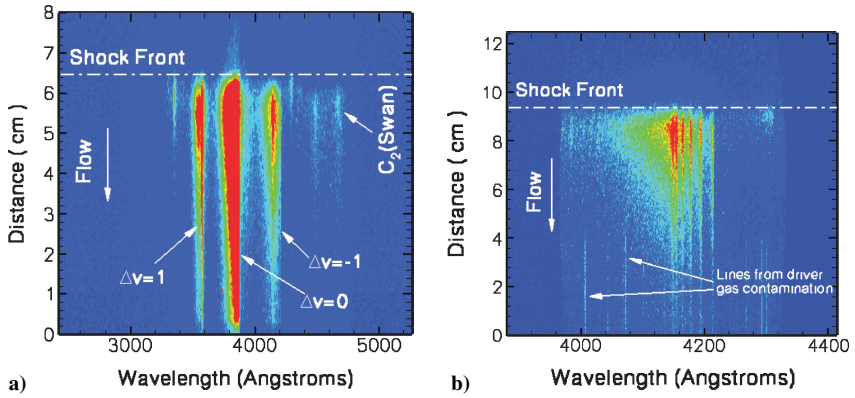

Fig. 5 Spectrograph samples of intensity variations with distance and wavelength for a) 8.6% CH_4/91.4%N_2 shot with shock velocity 5.39 km/s and 13.3 Pa (0.1 torr) and b) fine resolution of $\Delta v = -1$ manifold of CN (violet) at 5%CH_4/95%N_2 shot with shock velocity 5.56 km/s at 13.3 Pa (0.1 torr).

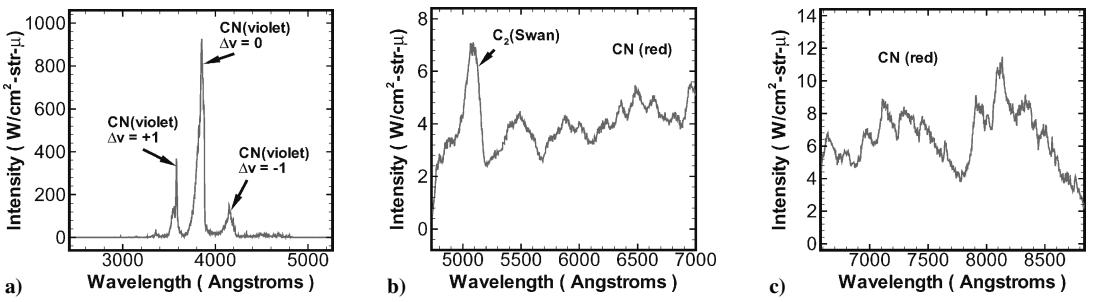

Fig. 6 Calibrated spectral scans in absolute units at various wavelengths derived from spectrograph images: a) and c) 8.6%CH_4/91.4%N_2, 5.39 km/s, 13.3 Pa (0.1 torr) and b) 8.6%CH_4/91.4%N_2, 5.56 km/s, 13.3 Pa (0.1 torr).

where the vector of conserved variables $\boldsymbol{U}$, the flux vector $\boldsymbol{F}$, and the source term vector $\boldsymbol{W}$ are given by

$$\boldsymbol{U} = \begin{Bmatrix} \rho_s \\ \rho u \\ E_{vs} \\ E \end{Bmatrix} \qquad \boldsymbol{F} = \begin{Bmatrix} \rho_s u \\ \rho u^2 + p \\ E_{vs} u \\ (E+p)u \end{Bmatrix} \qquad \boldsymbol{W} = \begin{Bmatrix} \dot{w}_s \\ 0 \\ \dot{w}_{Evs} \\ \dot{w}_E \end{Bmatrix} \tag{2}$$

In the code, the solution is advanced using a fourth-order Runge–Kutta algorithm. Conservation of mass, momentum, and total energy are assured during the solution procedure.

The source term vector $\boldsymbol{W}$ is computed using the same physical models in place for multidimensional DPLR calculations. The flow is assumed to be in thermal nonequilibrium, with separate energy equations solved for the total, E, and vibrational energies E_{vs}. An average vibrational energy equation is solved to represent the vibrational nonequilibrium of all polyatomic species. In this formulation, it is also assumed that the translational and rotational energy modes of the gas remain in equilibrium with each other. Vibrational relaxation is modeled using a Landau–Teller formulation, where relaxation times are fit to the expression from Millikan and White.[24] The correction term of Park[8] is added to the Landau–Teller formulation to prevent unphysically fast vibrational relaxation times at high temperature. A limiting cross section of $3 \times 10^{-21}\,\mathrm{m}^2$ is used for all polyatomic species. Characteristic vibrational temperatures for the simple harmonic oscillator approximation are taken from Gurvich et al.[25] Chemical kinetics are modeled using a 21-species (CH_4, CH_3, CH_2, HCN, N_2, N_2+, C_2, H_2, CH, NH, CN, CN+, N, N+, C, C+, H, H+, Ar, Ar+, e) 34-reaction finite-rate chemistry model developed by Gökçen specifically for Titan entry applications.[26] The governing temperature for all dissociation reactions is assumed to be $T_a = \sqrt{(TT_v)}$, whereas all recombination and exchange reactions are assumed to be governed by the translational temperature T (Ref. 8). A separate electron temperature is not considered, instead T_e is assumed equal to translational–rotational temperatures ($T = T_r$). Preferential dissociation from the higher vibrational levels is not modeled; all polyatomic species are assumed to be created and destroyed at the mixture vibrational temperature. Species thermodynamic properties are modeled using the curve-fit expressions of Gordon and McBride.[27] As a consistency check, it was verified that the thermochemical equilibrium state was the same as predicted by the Chemical Equilibrium with Applications (CEA) code of Gordon and McBride.[27] Figure 7 shows density and temperature profiles in the postshock obtained from the computations. CH_4 density is not shown because it immediately dissociates into smaller fragments such as CH, C, and H. The ionization level is found to be low (about 10^{-4}) and the dominant ion is N_2^+ or H^+ depending on the CH_4 concentration in the freestream. The CN mole fraction is about 10^{-2}, or lower in the cases with smaller CH_4 concentration. The vibrational relaxation appears rather quick in the 133.3 Pa (1 torr) case, whereas the 13.3 Pa (0.1 torr) case shows a vibrational relaxation zone of ~2 cm.

The shock-layer radiation along a given line of sight is calculated using the radiation code NEQAIR,[28] which computes the line-by-line emission, absorption, and transport. The CN spectroscopic constants, Frank–Condon factors, and transition moments are taken from the compilation of Laux,[29] where some of the data are taken from ab initio determinations by Bauschlicher et al.[30] In the baseline model, the higher electronic states of the radiating species (CN) are assumed to be populated according to a Boltzmann distribution, defined by an electronic temperature, which is assumed equal to the gas vibrational temperature. To simulate the intensity viewed by the spectrograph, a lateral line-of-sight calculation was done across the shock tube diameter (10.16 cm) at each axial station down the tube. The properties along the lateral lines of sight were assumed uniform along the diameter because boundary-layer effects were not simulated. Because the ICCD camera was open for a finite exposure time, these lateral intensity profiles were smeared based on an axial smear length given by the shock speed and the camera exposure time. It must be recognized that the flow in a shock tube is not strictly one dimensional. Variations in the direction normal to the tube axis may exist due to a boundary-layer growth and the wall effects in radiative transport causing uneven absorption in the radial direction. However, the boundary-layer thickness is expected to be small enough to only negligibly influence the flow speed.

IV. Nonlocal Collisional Radiative Model

Although a Boltzmann distribution of the CN excited state at the gas vibrational temperature was assumed in the baseline model, it will be evident at a later section that a collisional radiative model is needed to describe the true nonequilibrium populations of the excited CN molecules. Moreover, due to a very short radiative lifetime (62.5 ns) of CN (B) and possible nonlocal absorption, there is sufficient reason to believe that CN excitation and deexcitation processes are not solely governed by collisional processes. In fact the radiative processes in a shock tube (and also in flight), where the intensity field is far from a blackbody field, are likely to prevent the CN (B) state from ever reaching a local thermodynamic equilibrium. This phenomenon was earlier pointed out by Page and Arnold,[7] and is known as collisional limiting. CN (A) state, however, may reach

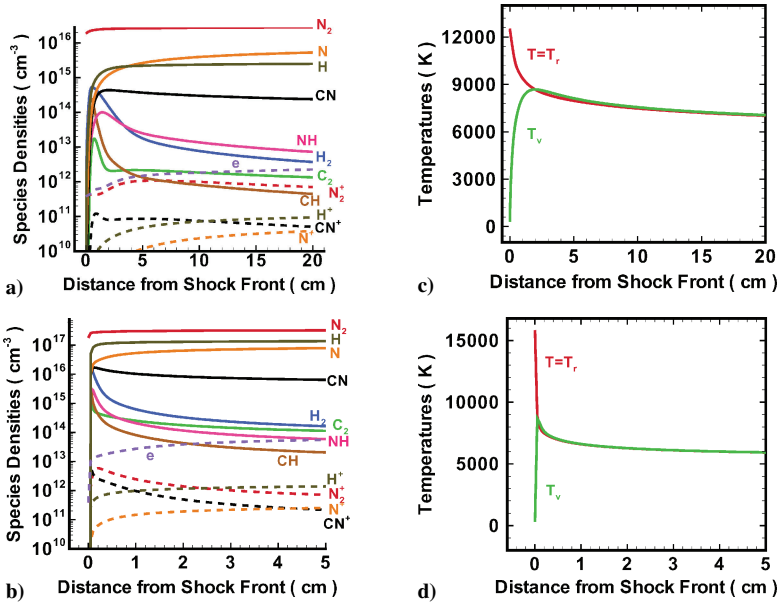

Fig. 7 Modeling results in the postshock region: a) species densities for 2% CH_4/98% N_2 at 5.15 km/s and 13.3 Pa (0.1 torr), b) species densities for 8.6% CH_4/91.4% N_2 at 5.93 km/s and 133.3 Pa (1.0 torr), c) translational–rotation and vibrational temperatures for 2% CH_4/98% N_2 at 5.15 km/s and 13.3 Pa (0.1 torr), and d) Translational–rotational and vibrational temperatures for 8.6% CH_4/91.4% N_2 at 5.93 km/s and 133.3 Pa (1.0 torr).

equilibrium collisionally with the ground state, CN (X), due to its longer radiative lifetime (8 μs). Also, there is evidence[31] that suggests mixing of CN (A) and CN (X) states, which if important, would enhance nonradiative transfer between these states and promote a Boltzmann population for the CN (A) state.

Nonequilibrium populations can be modeled, in principle, by writing a master equation for the number density that includes all relevant collisional and radiative processes that produce or consume a particular species of interest. However, in practice considerable simplifications are often necessary to make the model tractable.

A. Master Equation

The master equation for the conservation of CN (B) population is written as

$$\frac{\mathrm{d}n_{\mathrm{CNB}}}{\mathrm{d}t} = \sum_M (k_{fM} n_M n_{\mathrm{CNX}} - k_{bM} n_M n_{\mathrm{CNB}} - k_{fHM} n_M n_{\mathrm{CNB}} + k_{bHM} n_M n_{\mathrm{CNH}} - k_{fiM} n_M n_{\mathrm{CNB}} + k_{biM} n_M n_e n_{\mathrm{CN+}}) - \frac{n_{\mathrm{CNB}}}{\tau_r} + \gamma_{h\nu}\, I_{h\nu} n_{\mathrm{CNX}} \tag{3}$$

The number density of species s is denoted by n_s and M represents a generic collision partner (including electrons and heavy particles). The excitation rate constant of CN (X) with M as the collision partner is represented by k_{fM}, and k_{bM} is the same for the reverse process. The ground electronic state of CN is represented by X. The rate constant k_{fHM} is for the excitation of CN (B) to a generic higher state represented by H, and k_{bHM} is the rate constant of the reverse process. Similarly, k_{fiM} is the rate constant of the ionization process from the CN (B) state. The radiative lifetime of CN (B) is τ_r, and $\gamma_{h\nu}$ is the absorption rate constant for a given intensity $I_{h\nu}$ in the relevant wavelength range needed to excite CN (X) to CN (B). The processes considered in Eq. (3) are described in the order they appear on the right-hand side: 1) collisional excitation of CN (X) into CN (B), 2) collisional deexcitation from CN (B) to CN (X), 3) collisional excitation from CN (B) state to a generic higher state denoted by CN (H), 4) collisional deexcitation from a higher state CN (H) to CN (B), 5) Electron or heavy particle impact ionization from the CN (B) state, 6) electron CN+ recombination into CN (B) state, 7) radiative deexcitation due to spontaneous emission from the CN (B) state, and 8) radiative excitation from the CN (X) state to CN (B) state due to absorption.

Conceivably there are other processes that exist, such as reactive collisions that may produce or consume CN (B) from $N_2 + C$ collisions, $C + N$ recombination, photoionization, etc. Such reactive collisions are ignored due to lack of sufficient information on the reaction pathways leading to CN (B) state. However, they might have to be included if the experimental data points to the importance of such pathways. Photoionization of CN (B) is ignored due to nonavailability of photons in the energy range close to the ionization threshold (10–20 eV). Radiative transitions from higher electronic states have also been ignored due to the lack of any observed emissions from such transitions. Also, because transitions between B and A states are optically forbidden, collisional processes resulting in transitions between these states have been assumed to occur with low probabilities and are not included in the master equation.

We further simplify Eq. (3) based on the fact that CN (B) state has a very short radiative lifetime (62.5 ns) and that the ionization level at relevant conditions [5–6 km/s, 13.3–133.3 Pa (0.1–1.0 torr)] is low ($n_e/n_0 \sim 10^{-4}$). This allows us to neglect processes 3–6 leaving us with

$$\frac{\mathrm{d}n_{\mathrm{CNB}}}{\mathrm{d}t} = \sum_M (k_{fM} n_M n_{\mathrm{CNX}} - k_{bM} n_M n_{\mathrm{CNB}}) - \frac{n_{\mathrm{CNB}}}{\tau_r} + \gamma_{h\nu}\, I_{h\nu} n_{\mathrm{CNX}} \tag{4}$$

In Eq. (4), convection due to gas flow and diffusion has been ignored because of their larger timescales (microseconds) compared to the radiative timescale. In a steady state, Eq. (4) is rearranged as

$$\frac{n_{\mathrm{CNB}}}{n_{\mathrm{CNX}}} = \left(\gamma_{h\nu}\, I_{h\nu} + \sum_M k_{fM} n_M\right) \Big/ \left(\frac{1}{\tau_r} + \sum_M k_{bM} n_M\right) \tag{5}$$

From the detailed balance of collisional processes,

$$k_{fM}/k_{bM} = (n_{\mathrm{CNB}}/n_{\mathrm{CNX}})^* = \exp(-h\nu/kT) \tag{6}$$

In Eq. (6), the ratio of rovibrational partition functions is ignored (assumed close to unity) for simplicity at current temperatures because the spectroscopic constants of the X and B states are not very different. The asterisk represents the equilibrium composition, and $h\nu$ is the energy difference from the ground vibrational state of CN (B) to that of CN (X). Both B and X states have the same degeneracy of 2. Equation (5) can now be written as

$$\frac{n_{\mathrm{CNB}}}{n_{\mathrm{CNX}}} = \left(\gamma_{h\nu}\, I_{h\nu} + \sum_M k_{fM} n_M\right) \Big/ \left[\frac{1}{\tau_r} + \sum_M k_{fM} n_M \exp\left(\frac{h\nu}{kT}\right)\right] \tag{7}$$

Equation (7) will be called the nonlocal collisional radiative (CR) model throughout the rest of this paper and will be solved as a postprocessing step to the fluid dynamics solution, which gives the temperatures and species densities. The rates of the reactions are taken from Zagolin et al.,[18] who estimated them from their shock tube measurements of N_2/CO_2/Ar mixtures. Table 1 shows the rates used. For the case where net absorption is much smaller than the emission and the excitation rate coefficients can be written in the form $k_{fM} = A_M \exp(-h\nu/kT)$, Eq. (7) can be further simplified,

$$\frac{n_{\mathrm{CNB}}}{n_{\mathrm{CNX}}} = \left[\sum_M A_M n_M \Big/ \left(\frac{1}{\tau_r} + \sum_M A_M n_M\right)\right] \exp\left(-\frac{h\nu}{kT}\right) \tag{8}$$

Equation (8) clearly shows that the density of CN (B), and as a consequence, the emission power, varies exponentially with $1/T$. This formula will be used later to interpret the measured emission profiles. It appears that Zagolin et al.[18] also used a similar equation, although without the nonlocal absorption, to solve for densities of excited states. The master equation of Park,[13] on the other hand, included excitation and deexcitation only due to electron impact and radiation with a quasi-steady state and an optically thin gas assumption.

B. Absorption and Radiative Transport

When absorption is important, Eq. (7) becomes nonlocal because $I_{h\nu}$, the intensity field, depends on the emission and the absorption properties of the gas in the entire shock tube. Hence, this equation must be solved iteratively, which will be discussed in the next section. In this section, we discuss the technique used to evaluate the $\gamma_{h\nu} I_{h\nu} n_{\mathrm{CNX}}$ term, the rate of excitation of CN (X) to CN (B) due to absorption from the radiation field in the shock tube. In general, $\gamma_{h\nu}$ can be evaluated from the detailed balance between emission and absorption processes. However, such a method requires rovibrational line-resolved calculations because vibrational and rotational modes may be described by different temperatures. Because NEQAIR, which is a line-by-line radiation code, already performs this calculation for a given line of sight, we extract this information from the computed intensity and emission profiles. Moreover, the CN (B–X) band does not overlap with any other significant system

Table 1 Rate constants of collisional excitation estimated by Zagolin et al.[18]

Process	Rate constants, $\mathrm{cm}^3/\mathrm{mol}\cdot\mathrm{s}$
$\mathrm{CN\ (X)} + M \rightarrow \mathrm{CN\ (B)} + M$[a]	$1.80 \times 10^{11} T_a^{0.5} \exp(-37000/T_a)$[b]
$\mathrm{CN\ (X)} + \mathrm{e} \rightarrow \mathrm{CN\ (B)} + \mathrm{e}$	$6.25 \times 10^{14} T_a^{0.5} \exp(-37000/T_a)$
$\mathrm{CN\ (X)} + M \rightarrow \mathrm{CN\ (A)} + \mathrm{M}$	$1.50 \times 10^{11} T_a^{0.5} \exp(-13300/T_a)$
$\mathrm{CN\ (X)} + \mathrm{e} \rightarrow \mathrm{CN\ (A)} + \mathrm{e}$	$6.00 \times 10^{14} T_a^{0.5} \exp(-13300/T_a)$

[a]Heavy particle. [b]T_a used here T_a is assumed to be $\sqrt{(T T_v)}$.

under the current conditions, which allows us to assume that most absorbed power in this wavelength range goes toward exciting CN (X) to CN (B). (N_2^+ first negative signal is negligible.) Therefore, to a good approximation,

$$\gamma_{h\nu} I_{h\nu} n_{\mathrm{CNX}} \approx \frac{\text{absorption rate}}{h\nu} \tag{9}$$

The absorption rate (in watts per cubic centimeter) at a given point can be determined from NEQAIR by averaging absorption rates over all lines of sight passing through the point as shown in Fig. 8. Here $h\nu$ is in joules. Because we assume that the gas properties are uniform in the radial direction, essentially only one line of sight has to be calculated for emission and absorption properties. The remaining lines of sight just require numerical integration with the cell lengths adjusted by the line inclination factor. This transport calculation, however, has to be done separately for each wavelength because the absorption property of the gas changes with wavelength. In this work, we perform these transport calculations for several wavelength ranges of 100 Å wide over which the absorption and emission properties are averaged and are assumed constant for transport calculations.

For simplicity, we also assume that the shock tube walls are perfect reflectors and that the lines of sight are reflected specularly. The inside of the shock tube is polished aluminum, which is not a perfect mirror, and thus, some diffuse reflection and wall absorption may be present. Modeling a diffuse reflector is considerably more difficult and has been ignored in this work. We argue that because the absorption is expected to be smaller than the emission and collisional excitation terms in the number density balance equation of CN (B), the overall analysis may suffer from only a small error due to these assumptions. More important, the errors caused by these assumptions can be bounded, as will be shown later.

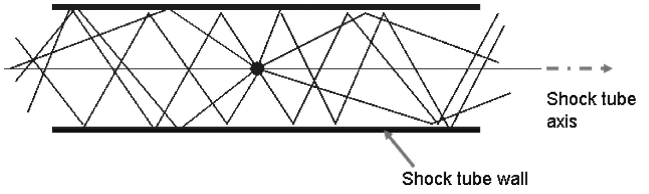

Fig. 8 Schematic of sample lines of sight passing through point due to internal reflections in shock tube.

The absorption in each cell along a line of sight is evaluated from the intensity I_λ (W/cm2-str-μ) and emission E_λ (W/cm3-str-μ) profiles,

$$\text{absorption}\,(\mathrm{W/cm^3\text{-}str\text{-}}\mu) = \frac{\mathrm{d}I_\lambda}{\mathrm{d}x} - E_\lambda \tag{10}$$

The derivative of the intensity is taken across the width of the cell. The absorption power (in watts per cubic centimeter) per unit volume is computed by summing over all lines of sight passing through the point, that is, integrating over the solid angle ω,

$$\text{absorption power} = \iint \left(\frac{\mathrm{d}I_\lambda}{\mathrm{d}x} - E_\lambda \right) \mathrm{d}\omega\, \mathrm{d}\lambda \tag{11}$$

Figure 9 shows the emission and absorption powers in the shock tube. It is assumed that the radiation from the shock tube driver gas is not absorbed in the uncontaminated postshock region. Also, it has been verified that the radiation from the driver arc is essentially nonexistent by the time the shock arrives in the test section. Figure 9 shows that the absorption power is anywhere between 25 and 50% of the emission power. A partially reflecting shock tube wall would reduce these estimates and the diffuse reflector would flatten the absorption profiles. In this analysis, however, such effects are ignored. The ratio of absorption to emission increases, as expected, with an increase in CH_4, and consequently CN, density, which goes up due to an increased CH_4 concentration in the gas and, in the case of Fig. 9d, due to a rise in pressure. Also, the nonlocal nature of absorption, which causes the emission from the brighter regions of the shock layer to be absorbed in the darker regions, disproportionately increases absorption power in the darker regions.

C. Solution Technique

Because of the nonlocal nature of the collisional radiative master equation (7), an iterative solution technique is necessary. We begin with the CFD solution that generates the one-dimensional profiles of the postshock densities and temperatures. When absorption is neglected, a first estimate of the CN (B) density is computed. This estimate of the excited state density is fed into NEQAIR along with flowfield properties to obtain the emission and absorption rate profiles along the tube axis, similar to the curves shown in Fig. 9. Using

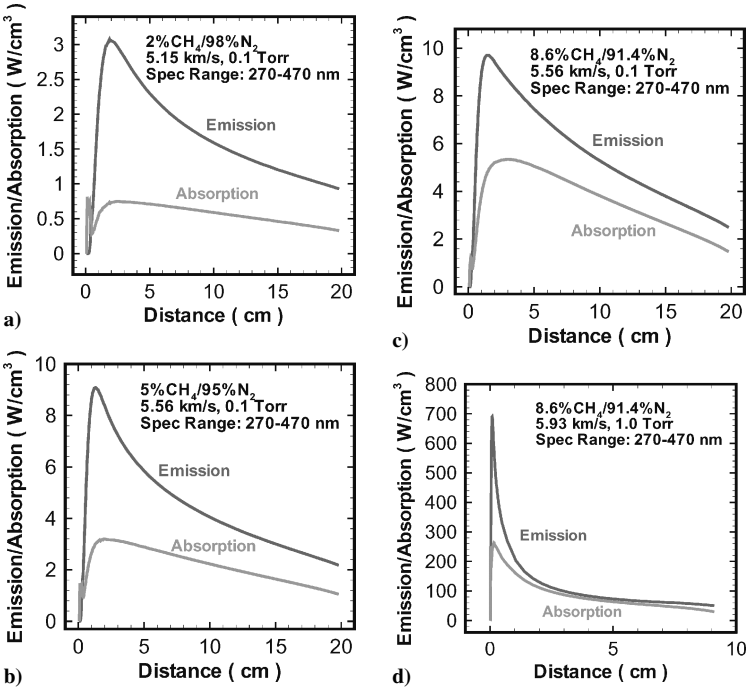

Fig. 9 Computed emission and absorption powers (watts per cubic centimeter) along the shock tube axis obtained from modeling results using nonlocal radiative transport for various shots.

this absorption rate and the methodology outlined in the preceding section, we solve Eq. (7) to get a refined estimate of CN (B) density. This process is repeated several times until self-consistency between the excited state density and the intensity field is obtained. The iteration process is shown schematically in Fig. 10. During each iteration, the CN (B) density and the intensity field are refined. Figure 11 shows the evolution of the emission and absorption profiles along the tube axis with iteration. Typically a self-consistent solution is obtained in about 5–6 iterations.

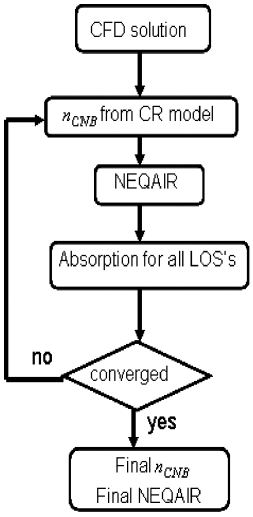

Fig. 10 Algorithm used to obtain self-consistent solution of the nonlocal collisional radiative model.

V. Comparisons with Experiment

In this section, we compare the intensity profiles computed with various models to the calibrated spectrograph measurements. These comparisons are done in absolute units (W/cm^2-str) with no normalization factors applied to any of the data sets. The calibrated experimental data, therefore, provide validation for not only the intensity rise and decay timescales, but also the absolute intensities predicted by the models. To be consistent, the model curves were smeared to compensate for the finite exposure time of the camera used in the experiments. The results are presented in Fig. 12 for four different shots: three shots at 13.3 Pa (0.1 torr) with three different CH_4 concentrations, 2, 5, and 8.6% by mole, balance N_2, and one shot at high pressure of 133.3 Pa (1 torr) with 8.6% CH_4 concentration. All cases have slightly different shock speeds, as shown in Fig. 12. Figures 12a–12d each presents four solid curves, one curve represents the experimental intensity profile, whereas the other three curves show the results from three different modeling approaches. The first one is labeled Boltzmann, which assumes that the CN excited states are populated according to a Boltzmann distribution characterized by the gas vibrational temperature, as described in the baseline model. The second curve shows the results of the nonlocal collisional radiative (CR) model [Eq. (7)] described earlier. The third curve is the collisional radiative model that is essentially Eq. (7), but without a nonlocal absorption term (CRT). The difference between the CR and CRT curves shows the importance of nonlocal absorption in determining the CN (B) population. The horizontal lines represent the equilibrium radiation levels. The intensity level when complete thermodynamic equilibrium (CTE) exists, that is, all species are in chemical equilibrium and all energy

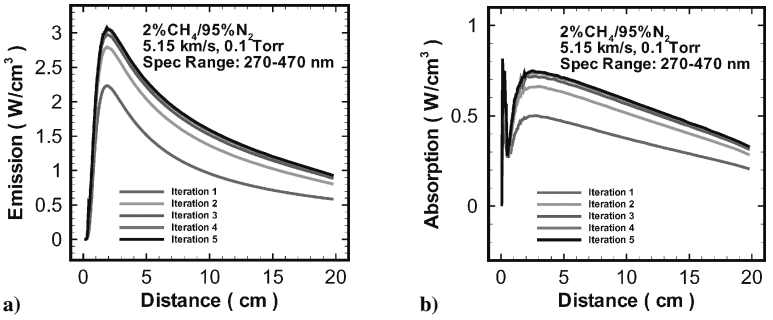

Fig. 11 Convergence of a) emission and b) absorption powers during the iterative process of obtaining self-consistent solution.

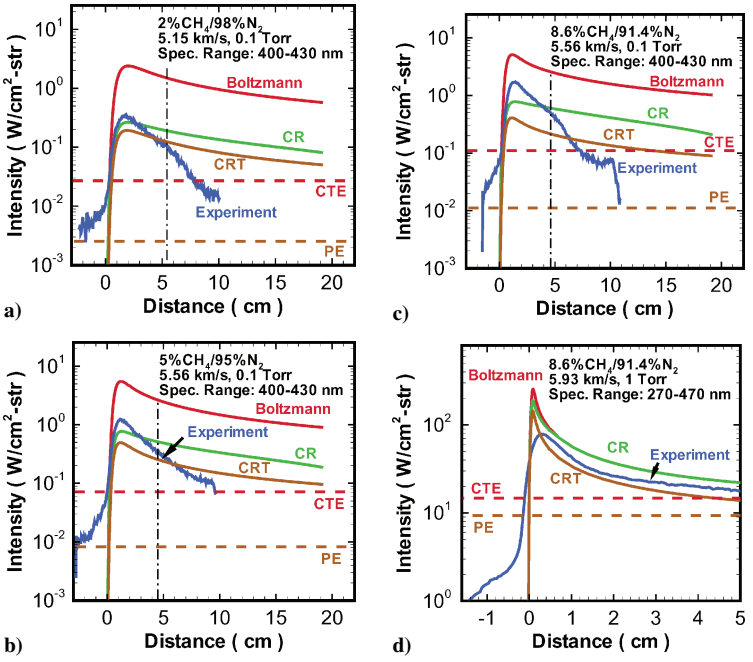

Fig. 12 Modeling and experimental profiles of CN (violet) intensities at a) 0.1 Torr, 2% CH_4, b) 0.1 Torr, 5% CH_4, c) 0.1 Torr, 8.6% CH_4, and d) 1.0 Torr, 8.6% CH_4. The vertical lines represent the arrival of the driver gas contamination.

states are described by a Boltzmann distribution with a single temperature is shown. However, because radiation plays a significant role in defining the populations of the excited states, especially CN (B), and the intensity field is not likely to reach equilibrium (a blackbody field), a (CTE) may never be achieved in such a device. Hence, we also define a partial equilibrium (PE) line. In (PE), no radiative equilibrium exists, but all species are in chemical equilibrium. The (PE) line without nonlocal absorption is the lowest intensity level possible within the test section. In the shots shown here, this level is never reached within the test time. The test time is shown by the vertical line, beyond which the experimental data are not considered useful due to driver gas contamination.

Figures 12 show that the Boltzmann assumption overpredicts the shock layer intensity by a factor of 3–7 at lower pressure [13.3 Pa (0.1 torr)], whereas the collisional radiative models predict intensities that are lower and in general closer to the experimental peak. This occurs primarily because the collisional radiative models account for radiative depopulation of the CN (B) state. CN (B) has a very short radiative lifetime (62.5 ns), which is smaller than all electron–CN (B) collision times assuming a fractional ionization of 10^{-4}. The timescale disparity disturbs the collisional equilibration process necessary to achieve a Boltzmann population of CN (B) state. In principle, the detailed balance of radiative processes (reabsorption of nonlocal emission) can also populate CN (B) with a Boltzmann distribution; however, that requires an intensity field of a blackbody, which does not exist in a shock tube, nor will it exist in flight. As a result, spontaneous emission that deexcites CN (B) occurs faster than the excitation due to absorption. This effect is termed by Page and Arnold[7] as collision limiting. In the high- pressure shot, this effect is minimized, as evident from Fig. 12d, due to more frequent collisions.

The effect of absorption in determining the CN (B) population can be seen in the difference between the CR and CRT curves. As CH_4 concentration goes up, while the pressure stays constant, the absorption increases due to higher CN emission. Also, as seen in Fig. 12, the absorption makes a larger fractional difference in the colder parts of the shock layer, that is, downstream. This effect occurs because of the downstream absorption of the upstream emission, which makes a larger fractional rise in the CN (B) population.

VI. Remaining Disagreements and Possible Reasons

It is obvious from Fig. 12 that although the peak intensity profiles in the shock layer are predicted within a factor of two, the fall-off rates of the intensity are significantly underpredicted by the models in the low-pressure shots [13.3 Pa (0.1 torr)]. Figure 13 shows the experimental fall-off rates of intensities of CN (red) and CN (violet) systems. For simplicity, we will ignore the nonlocal absorption in this section because it does not alter the fall-off rates significantly, as seen in Fig. 12. If collisional deexcitation of CN (B) is neglected, which is a good approximation in the 13.3 Pa (0.1 torr) case, the CN (B) fall-off rate can be written as

$$\frac{\mathrm{d}\,\ell n(n_{\mathrm{CNB}})}{\mathrm{d}x} = -D_B \frac{\mathrm{d}}{\mathrm{d}x}\left(\frac{1}{T}\right) + \frac{\mathrm{d}\,\ell n(n_{\mathrm{CNX}})}{\mathrm{d}x} + \frac{\mathrm{d}\,\ell n(n_M)}{\mathrm{d}x} \qquad (12)$$

where M is is the collisional partner that is predominantly responsible for CN (X) excitation to CN (B). If more than one collisional partner dominates, n_M can be treated as the density of the average collision partner. For a direct collisional excitation of CN (X) without an intermediate high lying transition state, D_B is the energy gap between B and X states of CN.

For CN (A) density, a similar expression can be derived by assuming that the CN (A) is predominantly produced via excitation from CN (X). However, in the case of CN (A), the radiative lifetime is comparable to the collisional deexcitation time and the gas flow time (which are all in the range of a few microseconds for the 0.1 torr case) and, hence, must be included in the master equation. Therefore we may write

$$\frac{\partial(n_{\mathrm{CNA}})}{\partial t} + \frac{\partial(n_{\mathrm{CNA}}\,u)}{\partial x} = \sum_M (k_{fM} n_M n_{\mathrm{CNX}} - k_{bM} n_M n_{\mathrm{CNA}}) - \frac{n_{\mathrm{CNA}}}{\tau_r} \qquad (13)$$

where, u is the gas flow speed. If the convection term is approximated by using an appropriate flow timescale as n_{CNA}/τ_f, the CN (A) density variation in a steady state can be expressed as

$$\frac{n_{\mathrm{CNA}}}{n_{\mathrm{CNX}}} = \left[\sum_M A_M n_M \Big/ \left(\frac{1}{\tau_r} + \frac{1}{\tau_f} + \sum_M g_A A_M n_M\right)\right] \times \exp\left(-\frac{D_A}{T}\right) \qquad (14)$$

A_M is the preexponential factor for the collisional excitation rate constant, and g_A is the degeneracy factor between A and X states. The fall-off rate can now be written as

$$\frac{\mathrm{d}\,\ell n(n_{\mathrm{CNA}})}{\mathrm{d}x} = -D_A \frac{\mathrm{d}}{\mathrm{d}x}\left(\frac{1}{T}\right) + \frac{\mathrm{d}\,\ell n(n_{\mathrm{CNX}})}{\mathrm{d}x} + \frac{\mathrm{d}}{\mathrm{d}x}\,\ell n\left[A_M n_M \Big/ \left(\frac{1}{\tau_r} + \frac{1}{\tau_f} + g_A A_M n_M\right)\right] \qquad (15)$$

On comparing Eq. (15) with the fall-off rate equation for CN (B), we note that CN (A) fall-off has a weaker dependence on the density variation of n_M compared to that of CN (B). This indicates that CN (A) is closer to a local thermodynamic equilibrium with CN (X) as compared to CN (B), and the densities of the collisional partners are less influential. This result was also seen in the master equation modeling of Zagolin et al.[18]

Figure 13 shows that both CN violet and red intensities fall in a log-linear fashion within the test time, except in the 133.3 Pa (1 torr) shot, where it falls in the log-linear fashion only until it reaches what appears to be thermochemical equilibrium. This log-linear dependence is compatible with Eqs. (12) and (15) and the variations in the fall-off region observed in the modeling results, where densities vary log-linearly and $1/T$ varies almost linearly. To explain the possible reasons for a rapid fall-off in the experiments, we consider two cases. First, the fall-off is mostly due to the gradient in temperature [where first term dominates in Eqs. (12) and (15)] and, second, is due to density gradients [where second term dominates in Eqs. (12) and (15)]. The third term is unlikely to dominate because the overall heavy particle density is expected to rise with distance, unless electron collisions dominate and electrons recombine as they move downstream. This is not the case according to the model results. The gas is weakly ionized and the electron density rises to an equilibrium value in the intensity fall-off region (Figs. 7a and 7b).

Scenario 1

In the first scenario, when the first term dominates, the ratio of the slopes of the violet to red intensity should be roughly equal to $D_B/D_A = 2.78$, if direct collisional excitation is the dominant process, or if both states are in thermodynamic equilibrium. However, the data do not show that to be the case because the slopes of the violet and the red intensities are only about 20–25% different (Fig. 13). A rough estimate of the activation energies (D_A and D_B) for the CN (X) state to CN (B) state can be made by evaluating the temperature and density gradients from the modeling results in the fall-off region. Table 2 shows these estimates. Note that these estimates assume that the transition state in thermodynamic equilibrium with the ground state population at the local temperature and that the collisional deexcitation is small compared to radiative deexcitation. The second assumption is valid only in the 13.3 Pa (0.1 torr) case. The transition state activation energies obtained in Table 2 have much higher values than the energy gap of 3.199 eV between CN (B) and CN (X) states. Therefore, if the current premise holds true, CN (B) is expected to form via an intermediate high-energy state. It could also be the dissociated (C + N) or the ionized (e + CN+) states, but such states are not expected to be in thermodynamic equilibrium

Table 2 Estimated activation energies of collisional excitation of CN (X) to CN (B) if true first scenario

Term	2%CH_4/98%N_2 5.15 km/s, 0.1 torr	5%CH_4/95%N_2 5.56 km/s, 0.1 torr	8.6%CH_4/91.4%N_2 5.56 km/s, 0.1 torr
$\partial \ln (n_{CNX})/\partial x$, cm^{-1} [a]	−0.056	−0.065	−0.041
$\partial/\partial x\ (1/T)$, $eV^{-1}\ cm^{-1}$ [a]	0.031	0.031	0.029
$\partial \ln (n_{CNB})/\partial x$, cm^{-1} [b]	−0.357	−0.416	−0.396
Estimated activation energy D_B, eV	9.82	11.42	12.4

[a]From computations. [b]From experiment.

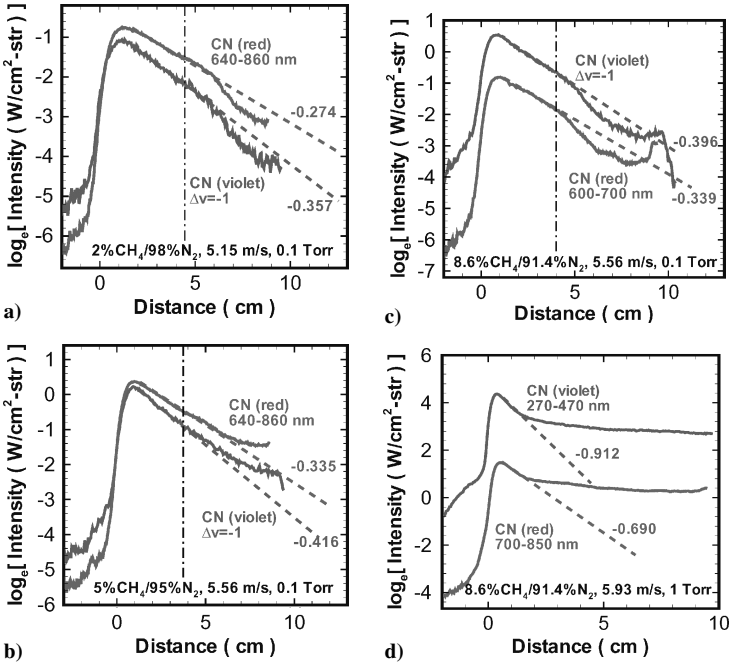

Fig. 13 Experimental intensity profiles for red and violet systems of CN showing fall-off rates in postshock region: vertical line, estimate of arrival of driver gas contamination; d) no arrival of driver gas during recorded time.

with the ground state CN (X) or whatever precursor species forms CN (B). The existence of such a state is, however, unlikely. This scenario is also unlikely because CN (A) state is expected to be close to a thermodynamic equilibrium with the CN (X) state, but the current intensity fall-off slope is too steep for that to be true.

Scenario 2

We now consider the second case, where the intensity fall-off is assumed to be due to density gradient, that is, the second term dominates in the fall-off region. In this scenario, the small difference in the slopes of the violet and red intensities is expected. Based on the data, we infer that both intensities fall-offs are probably dominated by the gradients in the CN (X) or the overall CN density. The slightly milder slope of the red intensity is either due to contribution of the temperature gradient term in Eqs. (12) and (15) or due to the gas flow convection, which only affects the red intensity profile due to its comparable radiative lifetime. In our opinion, given the current set of evidence, this scenario is more likely to be true for the following reasons:

1) It points to the fact that the gas phase CN consumption chemistry may be too slow, which is possible, given the uncertainties in the reaction rate data that have never been tested in such a rarified environment.

2) It appears from Figs. 7a and 7b that predicted C_2 density rises and drops by an order of magnitude very rapidly before the CN intensity reaches its peak, which is not evident from the C_2 (Swan) intensity variation seen in the spectrograph images. C_2 (Swan) and CN (violet) intensity, in Fig. 14, fall-off rates differ by only 13%. It is very likely that conversion of C_2 to CN via the following reactions in the current chemical kinetics model is too fast in the shock layer:

$$C_2 + N_2 \rightarrow 2CN \qquad C_2 + N \rightarrow CN + C \qquad (16)$$

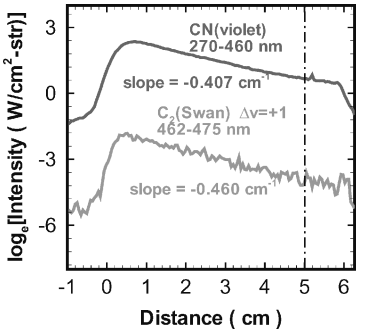

Fig. 14 Fall-off rates of CN (violet) and C_2 (Swan), $\Delta v = +1$, intensities for 8.6%CH_4/91.4%N_2 mixture at 5.39 km/s and 13.3 Pa (0.1 torr).

However, to show definitively which reactions rates determine the fall-off rates of CN in the shock layer, a Monte Carlo sensitivity analysis[32] is necessary, which will be the subject of future work. Additional reaction pathways may also be necessary to explain the observed fall-off trend. This finding does not necessarily invalidate the current chemical kinetic model developed by Gökçen,[26] it simply speaks to the extension of the model to such nonequilibrium regimes. In light of the new EAST data, it is worthwhile to refine the chemical kinetics model appropriate for the current conditions.

VII. Conclusions

The thermochemical models used to characterize the radiative heating environment for a Titan aerocapture maneuver is assessed based on detailed intensity measurements from shock tube testing. A new set of experiments conducted at the EAST facility at

NASA Ames Research Center at lower pressure [13.3–133.3 Pa (0.1 and 1 torr)], more representative of the heating environment than previous tests, provided calibrated spectrally and temporally resolved radiation intensity measurements over a wide wavelength range (200–880 nm).

The analysis presented shows that a Boltzmann distribution assumption for the CN electronic states leads to an overprediction of intensities by a factor of about 3–7 at 13.3 Pa (0.1 torr). It is shown that a Boltzmann population of the CN (B), which is responsible for the bulk of shock-layer radiation, cannot be sustained at low pressures due to a very short radiative lifetime (62.5 ns). Consequently, a nonlocal CR model for the excited states is developed. The proposed model includes solution of a simplified master equation for principal collisional and radiative transitions and nonlocal absorption within the shock tube. The prediction of the peak intensity overshoot falls within factor of two of the measured data. However, significant disparity remains in the intensity fall-off rates predicted by the models. Further analysis of the data and the relative fall-off rates of the CN (violet) and CN (red) intensities suggests that it is very likely that our current chemical kinetics model predict a slower CN consumption rate in the fall-off region than what is indicated by the measured profiles.

Further analysis is necessary to identify other possible reasons for the discrepancy and evaluate them to determine their likelihood. Also, a detailed Monte Carlo sensitivity analysis is needed to identify the key reaction rates that control the fall-off rates of the CN density and possibly recalibrate the chemical kinetics rates based on the current test data. In addition, the experimental data contains much more information than what was extracted in this work, such as vibrational and rotational temperatures, fall-off rates of other chemical species, and intensity rise times, which appear to be sensitive to vibrational relaxation rates. The data, with further investigation, could be utilized to assess the finer aspects of the current nonequilibrium thermochemical models.

The proposed nonlocal CR model and the iterative solution technique can be extended to flight environment computations to improve the radiative heating predictions. The predictions, however, could be further improved by addressing the uncertainties due to ground-to-flight traceability, namely, radiative transport with partial reflections and absorption at the shock tube walls, etc.

Acknowledgments

This work was funded by the In-Space Propulsion program under Task Agreement M-ISP-03-18 to NASA Ames Research Center. The work performed by D. Bose, D. W. Bogdanoff, and G. A. Allen is supported by the Prime Contract NAS2-99092 to ELORET. We would like to thank D. Prabhu (ELORET), D. Kontinos (NASA), J. O. Arnold (University of California, Santa Cruz), S. Sharma (NASA), T. R. Govindan (NASA), J. Olejniczak (NASA), T. Gökçen (ELORET) and David Hash (NASA) for useful discussions and suggestions to improve the manuscript. We also thank the Thermophysics Facilities Branch for expert maintenance and operation of the Electric Arc Shock Tube facility.

References

[1]Lockwood, M. K., "Titan Aerocapture Systems Analysis," AIAA Paper 2003-2799, July 2003.

[2]Justus, J., and Duvall, A., "Engineering Level Model Atmospheres for Titan and Neptune," AIAA Paper 2003-4803, July 2003.

[3]Takashima, N., Hollis, B., Zoby, E., Sutton, K., Olejniczak, J., Wright, M., and Prabhu, D., "Preliminary Aerothermodynamics Analysis of Titan Aerocapture Aeroshell," AIAA Paper 2003-4952, July 2003.

[4]Olejniczak, J., Wright, M., Prabhu, D., Takashima, N., Hollis, B., Zoby, E., and Sutton, K., "An Analysis of the Radiative Heating Environment for Aerocapture at Titan," AIAA Paper 2003-4953, July 2003.

[5]Olejniczak, D., Prabhu, D. K., Bose, D., and Wright, M. J., "Aeroheating Analysis for the Afterbody of a Titan Probe," AIAA Paper 2004-0486, Jan. 2004.

[6]Wright, M. J., Bose, D., and Olejniczak, J., "The Impact of Flowfield-Radiation Coupling on Aeroheating for Titan Aerocapture," *Journal of Thermophysics and Heat Transfer*, Vol. 19, No. 1, 2005, pp. 17–27.

[7]Page, W. A., and Arnold, J. O., "Shock Layer Radiation of Blunt Bodies at Reentry Velocities," NASA TR R-193, April 1964.

[8]Park, C., *Nonequilibrium Hypersonic Aerothermodynamics*, Wiley, New York, 1990.

[9]Laub, B., "Thermal Protection Concepts and Issues for Aerocapture at Titan," AIAA Paper 2003-4954, July 2003.

[10]Baillion, M., Taquin, G., and Soler, J., "Huygens Radiative Probe Environment," *Proceedings of the 19th International Symposium on Shock Waves*, Springer-Verlag, Berlin, 1995, pp. 339–346.

[11]Baillion, M., and Taquin, G., "Radiative Heat Flux: Theoretical and Experimental Predictions for Titan Entry Probe," *Capsule Aerothermodynamics*, AGARD Rept. 808, May 1997.

[12]Baillion, M., Pallegoix, J. F., and Soler, J., "Huygens Probe Aerothermodynamics," AIAA Paper 97-2476, July 1997.

[13]Park, C. S., "Studies of Radiative Emission from the Simulated Shock Layer of the Huygens Probe," Ph.D. Dissertation, Dept. of Aeronautics and Astronautics, Stanford Univ., Stanford, CA, 1991.

[14]Park, C. S., and Bershader, D., "Studies of Radiative Emission from the Simulated Shock Layer of the Huygens Probe," *Proceedings of the 18th International Symposium on Shock Waves*, Springer-Verlag, Berlin, 1992, pp. 671–676.

[15]Labracherie, L., Billiotte, M., and Houas, L., "Shock Tube Analysis of Argon Influence in Titan Radiative Environment," *Journal of Thermophysics and Heat Transfer*, Vol. 10, No. 1, 1996, pp. 162–168.

[16]Kpante, K.-K., Zeitoun, D., and Labracherie, L., "Computation and Experimental Validation of N_2–CH_4–Ar Mixture Flows Behind Normal Shock Wave," *Shock Waves*, Vol. 7, No. 6, 1997, pp. 351–361.

[17]Ramjaun, D., Dumitrescu, M., and Brun, R., "Kinetics of Free Radicals Behind Strong Shock Waves," *Journal of Thermophysics and Heat Transfer*, Vol. 13, No. 2, 1999, pp. 219–225.

[18]Zalogin, G., Kozlov, P., Kuznetsova, L., Losev, S., Makarov, V., Romanenko, Y., and Surzhikov, S., "Radiation Excited by Shock Waves in a CO_2–N_2–Ar Mixture: Experiment and Theory," *Technical Physics*, Vol. 71, No. 6, 2001, pp. 10–16.

[19]Sharma, S. P., and Park, C., "Operating Characteristics of a 60- and 10-cm Electric Arc-Driven Shock Tube, Part 1: The Driver," *Journal of Thermophysics and Heat Transfer*, Vol. 4, No. 3, 1990, pp. 259–265.

[20]Sharma, S. P., and Park, C., "Operating Characteristics of a 60- and 10-cm Electric Arc-Driven Shock Tube, Part 2: The Driven Section," *Journal of Thermophysics and Heat Transfer*, Vol. 4, No. 3, 1990, pp. 266–272.

[21]Sharma, S. P., and Gillespie, W. D., "Nonequilibrium and Equilibrium Shock Front Radiation Measurements," AIAA Paper 90-0139, Jan. 1990.

[22]Sharma, S. P., Gillespie, W. D., and Meyer, S. A., "Shock Front Radiation Measurements in Air," AIAA Paper 91-0573, Jan. 1991.

[23]Wright, M. J., Candler, G. V., and Bose, D., "Data-Parallel Line Relaxation Method for the Navier–Stokes Equations," *AIAA Journal*, Vol. 36, No. 9, 1998, pp. 1603–1609.

[24]Millikan, R. C., and White, D. R., "Systematics of Vibrational Relaxation," *Journal of Chemical Physics*, Vol. 39, No. 12, 1963, pp. 3209–3213.

[25]Gurvich, L., Veyts, I., and Alcock, C. (eds.), *Thermodynamic Properties of Individual Substances*, 4th ed., Hemisphere, New York, 1991.

[26]Gökçen, T., "N_2–CH_4–Ar Chemical Kinetic Model for Simulations of Atmospheric Entry to Titan," AIAA Paper 2004-2469, June 2004.

[27]Gordon, S., and McBride, B. J., "Computer Program for Calculation of Complex Chemical Equilibrium Compositions and Applications," NASA RP 1311, Oct. 1994.

[28]Whiting, E. E., Yen, L., Arnold, J. O., and Paterson, J. A., "NEQAIR96, Nonequilibrium and Equilibrium Radiative Transport and Spectra Program: User's Manual," NASA RP-1389, Dec. 1996.

[29]Laux, C. O., "Optical Diagnostics and Radiative Emission of Air Plasmas," High Temperature Gasdynamics Laboratory Rept. T-288, Stanford Univ., Stanford, CA, Aug. 1993.

[30]Bauschlicher, C. W., Langhoff, S. R., and Taylor, P. R., "Theoretical Study of the Dissociation Energy and the Red and Violet Systems of CN," *Astrophysical Journal*, Vol. 332, Sept. 1988, pp. 531–538.

[31]Kotlar, A. J., Field, R. W., Steinfeld, J. I., and Coxon, J. A., "Analysis of Perturbations in the A^2Pi-X^2Sigma^+ Red System of CN," *Journal of Molecular Spectroscopy*, Vol. 80, No. 1, 1980, pp. 86–108.

[32]Bose, D., Wright, M. J., and Gokcen, T., "Uncertainty and Sensitivity Analysis of Thermochemical Modeling for Titan Atmospheric Entry," AIAA Paper 2004-2455, Jan. 2004.